

Formation process of hydrocarbons in PDRs: gas phase chemistry or fragmentation of PAHs?

Maitraiye Tiwari (PhD student)

Prof. Dr. Karl Menten & Dr. Friedrich Wyrowski

Collaborators: J.P. Pérez-Beaupuits, M. -Y. Lee, W.-J. Kim

Max Planck Institute for Radioastronomy

mtiwari@mpifr-bonn.mpg.de

September 3, 2019

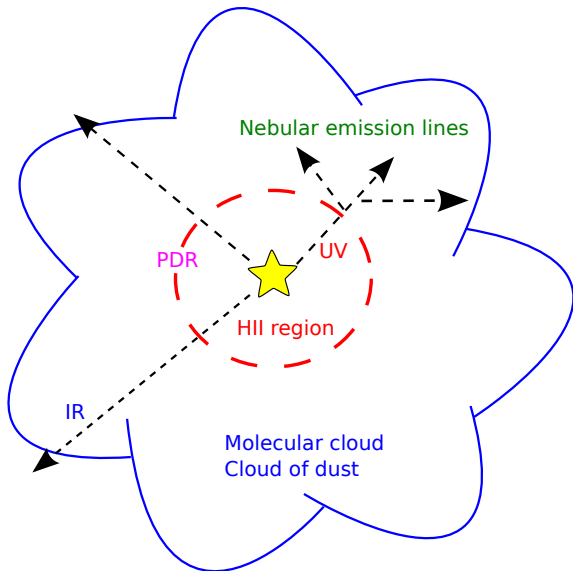


- Introduction
 - What are PDRs and HII regions?
 - Structure of a PDR
- M8
- Motivation
- Observations
- Results
 - Qualitative analysis: Spatial distribution
 - Quantitative analysis: LTE and non-LTE
 - Comparison with PDR models
- Conclusions

Introduction: What are HII regions and PDRs?

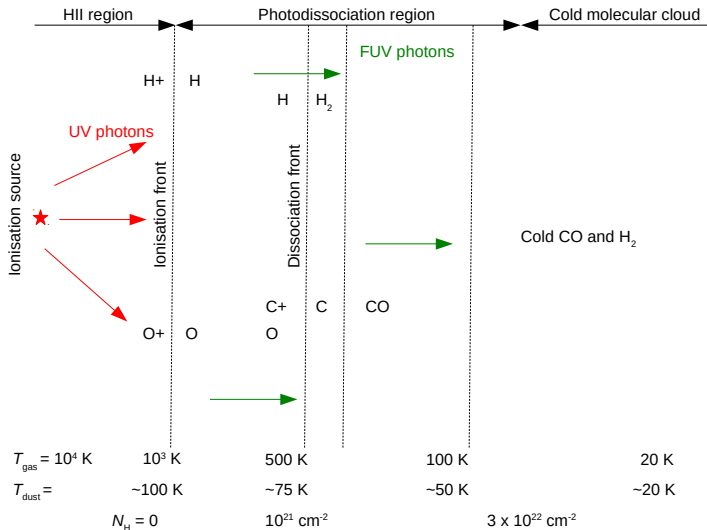
HII region: $h\nu > 13.6 \text{ eV}$

PDR: $6 \text{ eV} < h\nu < 13.6 \text{ eV}$



Introduction: Structure of a PDR

Giving rise to a rich hydrocarbon chemistry!



Adapted from Hollenbach & Tielens (1999) and Goicoechea et al. (2016).

The beautiful Lagoon Nebula (M8)...

- M8 hosts bright HII regions, PDRs and star-forming regions.
- It is 1.25 kpc away from us and lies in the Sagittarius-Carina arm.
- The second brightest CO emission detected toward Her 36 (White et al. 1997).

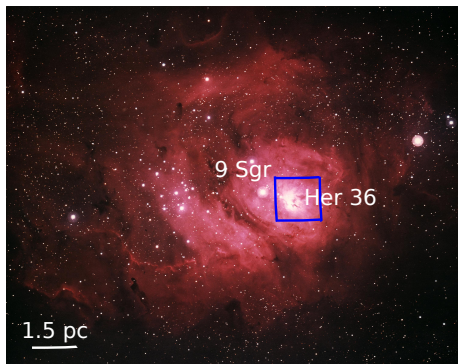


Image taken from National Optical Astronomy Observatory gallery

One of the most prominent PDRs in our Galaxy and yet explored very little.

Goals:

- To establish an inventory of hydrocarbons observed in M8.
- To probe the physical conditions of gas responsible for the hydrocarbon emission.
- What is the formation process of hydrocarbons? Gas phase chemistry or fragmentation of PAHs?

Motivation: formation of hydrocarbons in PDRs

Low UV flux PDRs with $G_0 < 100$ (in Habing units)

- hydrocarbon abundance: observed $>$ predicted by models.
- e.g. Horsehead Nebula (Teyssier et al. 2004).
- Fragmentation of PAHs by FUV photons? (Le Page et al. 2003, Pety et al. 2005, Montillaud et al. 2012).

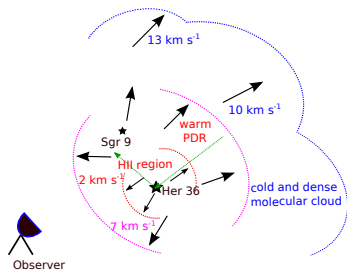
High UV flux PDRs with $G_0 \sim 10^4\text{--}10^5$ (in Habing units)

- hydrocarbon abundance: observed \sim predicted by models.
- e.g. the Orion Bar (Cuadrado et al. 2015).
- high temperatures in high UV flux PDRs lead to new gas phase routes (Cuadrado et al. 2015).

Testing ground: M8

A suitable laboratory to study hydrocarbons in high UV flux PDRs.

- M8 is among the highest UV flux ($G_0 \sim 10^5$) PDRs in our Galaxy.
- It has a face-on geometry with cold dense molecular cloud behind Her 36 and Sgr 9.
- The warm PDR veil is accelerated toward us.



(Tiwari et al. 2018)

Observations: IRAM 30m and APEX



**Atacama Pathfinder
EXperiment (APEX)**



**Institut de Radioastronomie
Millimétrique (IRAM)**

- **APEX:** Pointed observations and OTF mapping of the mid and high rotation transitions of C_2H and $c-C_3H_2$.
- **IRAM 30 m** Pointed observations and OTF mapping of the low rotation transitions of C_2H and $c-C_3H_2$.

Spectra: C₂H and c-C₃H₂

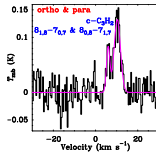
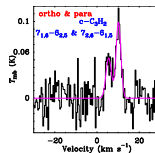
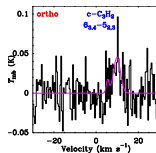
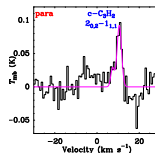
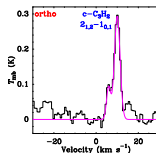
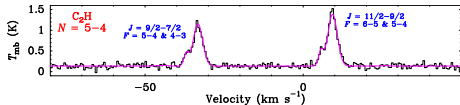
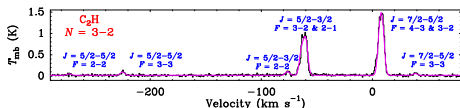
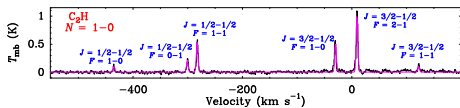
2 velocity components seen.

$N = 1 \rightarrow 0$: 6 hfs components

$N = 3 \rightarrow 2$: 8 hfs components

$N = 5 \rightarrow 4$: 4 hfs components

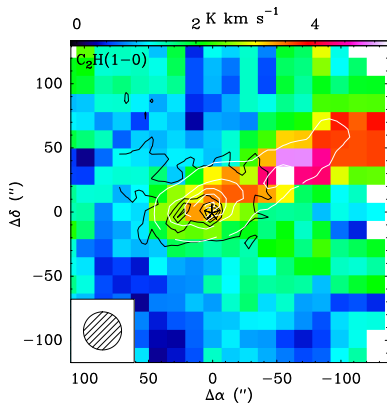
5 ortho and para transitions detected. 2 are blended.



(Tiwari et al. 2019)

Spatial distribution: Where are the PAHs?

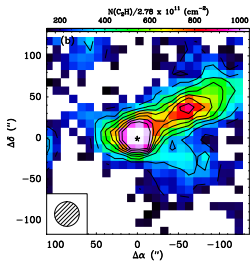
No clear spatial correlation between the emission from PAHs and C_2H emission.



- SPIRE 350 μm : white and 8 μm PAH: black
- SPIRE 350 μm follows the hydrocarbon emission distribution.
- 8 μm PAH emission does not follow it.

(Tiwari et al. 2019)

LTE Analysis

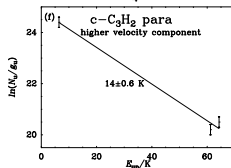
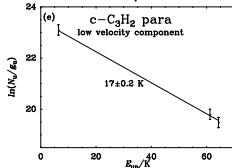
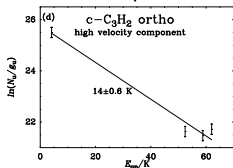
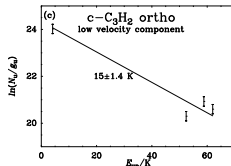
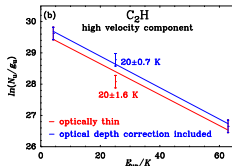
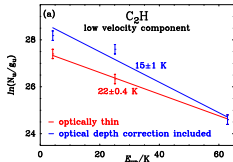


$N(\text{C}_2\text{H})$ optically thin $\sim (3.3 \pm 0.12) \times 10^{14} \text{ cm}^{-2}$

$N(\text{C}_2\text{H})$ opacity corrected $\sim (4.8 \pm 0.35) \times 10^{14} \text{ cm}^{-2}$

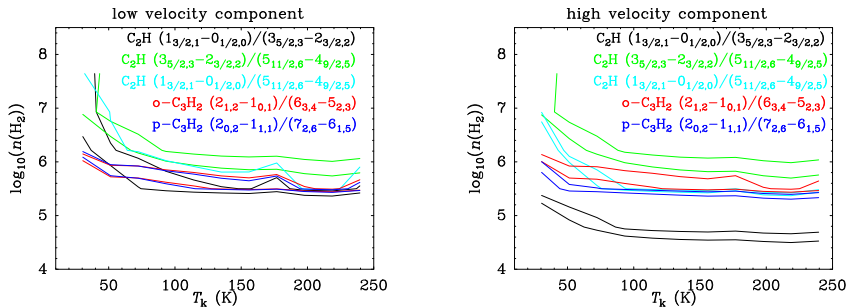
$N(\text{C}_3\text{H}_2)$ -ortho $\sim (2.2 \pm 0.44) \times 10^{13} \text{ cm}^{-2}$

$N(\text{C}_3\text{H}_2)$ -para $\sim (9.4 \pm 0.21) \times 10^{12} \text{ cm}^{-2}$



Non-LTE Radiative transfer modeling (RADEX)

velocity widths taken from the observed spectra
column densities taken from the LTE analysis



- Low-velocity comp. probes the PDR foreground veil $\sim 5 \times 10^5 - 5 \times 10^6 \text{ cm}^{-3}$.
- High-velocity comp. probes gas very close to Her 36 and also the background material $\sim 5 \times 10^4 - 5 \times 10^6 \text{ cm}^{-3}$.

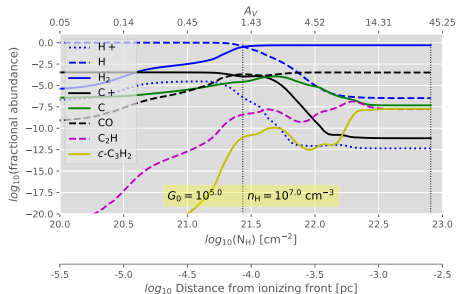
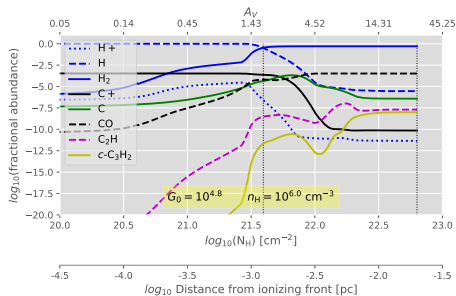
(Tiwari et al. 2019)

PDR models of Meijerink and Spaans 2005

- Semi-infinite slab geometry, irradiation from one side, homogeneous medium
- > 300 chemical species
- Photo-electric heating from PAHs and small dust grains, cosmic ray heating, collisional de-excitation of vib. excited H₂, etc.
- Cooling: IR emission of [C II], [O I], [C I], [S II], submm emission of CO, H₂O, H₂, OH, grain-grain collisions.

Output: abundances, column densities, temperatures, heating/cooling rates vs A_v , intensities and opacities.

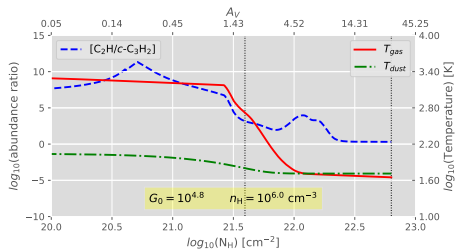
Modeling results



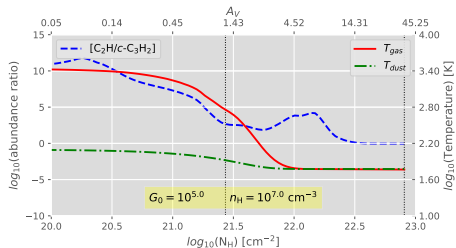
- Guided by G_0 (Tiwari et al. 2018) and $n(\text{H}_2)$ densities calculated by RADEX.
- We get $N(\text{C}_2\text{H})$ and $N(\text{c-C}_3\text{H}_2) \sim 3$ and $10\text{--}25$ times higher than obtained from observations.
- This difference can arise from unresolved clumpiness i.e. unaccounted for in the calculations based on our observations.

(Tiwari et al. 2019)

Modeling results



\log_{10} Distance from ionizing front [pc]



\log_{10} Distance from ionizing front [pc]

- The predicted average $T_{\text{gas}} \sim 100$ and 120 K, similar to $100\text{--}150$ K values found in Tiwari et al. (2018).
- The models did not include surface grain chemistry or PAH destruction mechanisms due to UV.
- Gas-phase chemistry is enough to explain the hydrocarbon abundances in high -UV flux PDRs.

(Tiwari et al. 2019)

Comparison with Orion Bar

Orion Bar is a dense (10^4 – 10^6 cm $^{-3}$, Peng et al. 2012) high UV flux (1.17×10^4) PDR.

The results for the Orion Bar are taken from Cuadrado et al. 2015

Species	Column densities $\log_{10}(N)$ (cm $^{-2}$)			
	Observed		PDR model	
	M8	Orion	M8	Orion
C $_2$ H	14.6	14.6	15	14.1–14.8
c-C $_3$ H $_2$	13.5	13.1	14.6–14.9	12.2–12.9

- The values are similar but the results predicted by models are different.
- Different characteristic features of the models.
- Meudon is a more sophisticated code that includes many desorption features, more cooling mechanisms, more dust properties, different chemical networks.

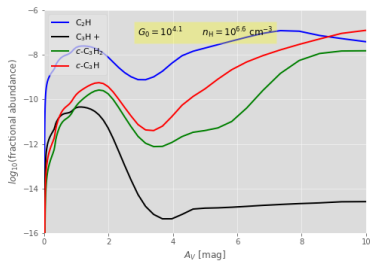
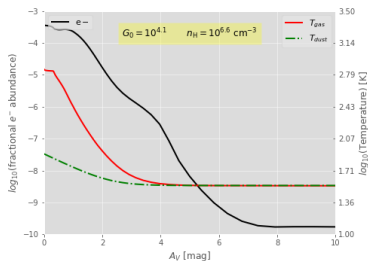
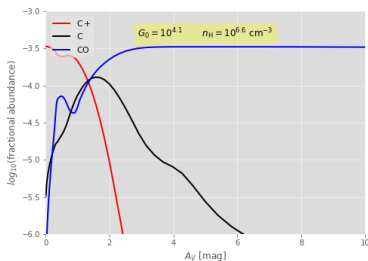
- We detected eighteen hfs components of C_2H and five transitions of ortho and para species of $c-C_3H_2$.
- We constrained H_2 volume densities $\sim 5 \times 10^4 - 5 \times 10^6 \text{ cm}^{-3}$ using non-LTE methods.
- Observed column densities $N(C_2H) \sim 5 \times 10^{14} \text{ cm}^{-2}$ and $N(c-C_3H_2) \sim 1 \times 10^{13} \text{ cm}^{-2}$.
- Predictions from PDR models match the observations reasonably well (factor of 3 and 10–25). Differences due to unresolved clumpiness in our data.
- Gas-phase chemistry is enough to explain hydrocarbon abundance in high-UV flux PDRs.

- We need to establish an inventory of hydrocarbons in M8.
- we also imaged the CH 0.5 and 1.4 THz lines using SOFIA in July 2018.
- ALMA observations to observe small hydrocarbons (which require better resolution and high signal/noise to get detected), in addition to C_2H and $c-C_3H_2$.

hfs in c2h: The energy levels are designated as N , J , and F . The coupling between the rotational angular momentum N and the unpaired electron spin S causes spin doubling ($J = N + S$), while the coupling of angular momentum J and spin of the hydrogen nucleus I results in hfs ($F = J + I$)

It has ortho and para symmetries owing to the two out of plane hydrogen atoms, which are equidistant from the C atoms. It is an oblate asymmetric top with b-type rotational transitions where the main selection rules are ΔK_a and $\Delta K_c = \pm 1$. The levels are ortho and para depending on the odd and even values of $K_a + K_c$ (for a more extensive description see).

extra slide-2



($G_0 = 1$ corresponds to a flux of $1.6 \times 10^{-3} \text{ erg cm}^{-2} \text{ s}^{-1}$)

extra slide 3: List of hydrocarbon observations

Species	Transition	Frequency (GHz)	E_{up}/k (K)	Instrument	n_{cr} (cm ⁻³)
C ₂ H	$N = 1 \rightarrow 0, J = 3/2 \rightarrow 1/2, F = 1 \rightarrow 1$	87.2841	4.2	IRAM 30m/EMIR	2.5×10^5
	$N = 1 \rightarrow 0, J = 3/2 \rightarrow 1/2, F = 2 \rightarrow 1$	87.3168	4.2	IRAM 30m/EMIR	3.2×10^5
	$N = 1 \rightarrow 0, J = 3/2 \rightarrow 1/2, F = 1 \rightarrow 0$	87.3285	4.2	IRAM 30m/EMIR	9.5×10^4
	$N = 1 \rightarrow 0, J = 1/2 \rightarrow 1/2, F = 1 \rightarrow 1$	87.4019	4.2	IRAM 30m/EMIR	1.1×10^6
	$N = 1 \rightarrow 0, J = 1/2 \rightarrow 1/2, F = 0 \rightarrow 1$	87.4071	4.2	IRAM 30m/EMIR	1.8×10^5
	$N = 1 \rightarrow 0, J = 1/2 \rightarrow 1/2, F = 1 \rightarrow 0$	87.4464	4.2	IRAM 30m/EMIR	2.2×10^5
	$N = 3 \rightarrow 2, J = 7/2 \rightarrow 5/2, F = 3 \rightarrow 3$	261.9781	25.1	APEX/PI230	3.2×10^4
	$N = 3 \rightarrow 2, J = 7/2 \rightarrow 5/2, F = 4 \rightarrow 3$	262.0042	25.1	APEX/PI230	8.7×10^5
	$N = 3 \rightarrow 2, J = 7/2 \rightarrow 5/2, F = 3 \rightarrow 2$	262.0064	25.1	APEX/PI230	8.5×10^5
	$N = 3 \rightarrow 2, J = 5/2 \rightarrow 3/2, F = 3 \rightarrow 2$	262.0649	25.1	APEX/PI230	8.9×10^5
	$N = 3 \rightarrow 2, J = 5/2 \rightarrow 3/2, F = 2 \rightarrow 1$	262.0674	25.1	APEX/PI230	8.2×10^5
	$N = 3 \rightarrow 2, J = 5/2 \rightarrow 3/2, F = 2 \rightarrow 2$	262.0789	25.1	APEX/PI230	1.2×10^5
	$N = 3 \rightarrow 2, J = 5/2 \rightarrow 5/2, F = 3 \rightarrow 3$	262.2086	25.1	APEX/PI230	8.4×10^4
	$N = 3 \rightarrow 2, J = 5/2 \rightarrow 5/2, F = 2 \rightarrow 2$	262.2509	25.1	APEX/PI230	4.9×10^4
	$N = 5 \rightarrow 4, J = 11/2 \rightarrow 9/2, F = 6 \rightarrow 5$	436.661	62.9	APEX/FLASH ⁺	2.9×10^6
	$N = 5 \rightarrow 4, J = 11/2 \rightarrow 9/2, F = 5 \rightarrow 4$	436.6618	62.9	APEX/FLASH ⁺	2.9×10^6
	$N = 5 \rightarrow 4, J = 9/2 \rightarrow 7/2, F = 5 \rightarrow 4$	436.723	62.9	APEX/FLASH ⁺	3.3×10^6
$N = 5 \rightarrow 4, J = 9/2 \rightarrow 7/2, F = 4 \rightarrow 3$	436.724	62.9	APEX/FLASH ⁺	3.2×10^6	
c-C ₃ H ₂ ortho	$J_{K_a, K_b} = 2_{1,2} \rightarrow 1_{0,2}$	85.3388	6.4	IRAM 30m/EMIR	1.1×10^6
	$J_{K_a, K_b} = 6_{3,4} \rightarrow 5_{2,3}$	285.7956	54.7	APEX/FLASH ⁺	8.4×10^6
	$J_{K_a, K_b} = 7_{1,6} \rightarrow 6_{2,5}$	284.998	61.2	APEX/FLASH ⁺	8.9×10^6
	$J_{K_a, K_b} = 8_{1,8} \rightarrow 7_{0,7}$	284.8052	64.3	APEX/FLASH ⁺	1.0×10^7
c-C ₃ H ₂ para	$J_{K_a, K_b} = 2_{0,2} \rightarrow 1_{1,1}$	82.0935	6.4	IRAM 30m/EMIR	9.9×10^5
	$J_{K_a, K_b} = 7_{2,6} \rightarrow 6_{1,5}$	284.9993	61.2	APEX/FLASH ⁺	1.0×10^7
	$J_{K_a, K_b} = 8_{0,8} \rightarrow 7_{1,7}$	284.8052	64.3	APEX/FLASH ⁺	1.0×10^7

Differences may arise due to distinct chemical networks used in both models. The Meudon code run by Cuadrado et al. (2015) uses a total of 130 species and 2800 gas-phase reactions. The Meijerink & Spaans (2005) model, on the other hand, uses a total of 309 species and 4453 gas-phase reactions. Also, unlike the Meudon code, our models do not distinguish between the c- and l-species of $c\text{-C}_3\text{H}_2$ leading to its higher column density prediction. Furthermore, it is worth mentioning that the Meudon code includes the updated state-to-state reactions of vibrationally excited H_2 with $[\text{C II}]$, $[\text{O I}]$, OH (Agúndez et al. 2010). It also has upgraded the carbon-bearing species network and used the most recent branching ratios for ion-molecule, neutral-neutral, dissociative recombination, and charge exchange reactions for carbon chains and hydrocarbon species as described in Chabot et al. (2013). These updates are missing in our PDR models. The actual impact of these exchange reactions cannot be measured until the PDR model by Meijerink & Spaans (2005) is updated.